Atomization efficiency and photon yield in laser-induced breakdown spectroscopy analysis of single nanoparticles in an optical trap

Pablo Purohit, Francisco J. Fortes and J. Javier Laserna*

Departamento de Química Analítica, Universidad de Málaga, Campus de Teatinos S/N,29071, Malaga (Spain) Email: laserna@uma.es

ABSTRACT: Laser-induced breakdown spectroscopy (LIBS) was employed for investigating the influence of particle size on the dissociation efficiency and the absolute production of photons per mass unit of airborne solid graphite spheres under single-particle regime. Particles of average diameter of 400 nm were probed and compared with 2 μm particles. Samples were first catapulted into aerosol form and then secluded in an optical trap set by a 532 nmlaser. Trap stability was quantified before subjecting particles to LIBS analysis. Fine alignment of the different lines comprising the optical catapulting-optical trapping-laser induced breakdown spectroscopy instrument and tuning of excitation parameters conditioning the LIBS signal such as fluence and acquisition delay are described in detail with the ultimate goal of acquiring clear spectroscopic data on masses as low as 75 fg. The atomization efficiency and the photon yield increase as the particle size becomes smaller. Time-resolved plasma imaging studies were conducted to elucidate the mechanisms leading to particle disintegration and excitation.

Keywords: Laser-induced breakdown spectroscopy, LIBS, Solid aerosols, Single particle analysis, Optical catapulting, Optical trapping, Atomization efficiency, Photon yield

1. Introduction

Determination of concentration, composition and size of atmospheric particulate matter is of crucial importance to ensure air quality and safety given their direct impact on the human organism.[1-2] Airborne particles are transported in aerosol form and can be classified according to aerodynamic diameter, which ultimately determines atmospheric lifetime and how much of a threat they pose to health, particularly to the respiratory system. Three main inhalable fractions are found: the coarse fraction or PM10 (particle diameter < 10 μm), the fine fraction or PM2.5 (particle diameter < 2.5 μm) and the ultrafine fraction (particle diameter < 100 nm). As size decreases, assimilation of particles becomes easier and deposition on lungs and other organs can exacerbate the symptoms of already existing diseases or originate new conditions. Carbon is one of the main components of particulate material.[3] Pure carbon compounds, known as black carbon (BC), of the fine and ultrafine fractions have been related not only to public health issues, but also to global climate change.[4-5] Black carbon may be of natural or anthropogenic occurrence. Fuel and biomass burning are deemed the most prominent sources of BC particles. General exposure to ultrafine aerosols of diverse chemical composition is also increasing from other human activities, e.g., the development of nanotechnology, potentially bringing along toxic effects that remark the need of controlling the presence of nanometric materials in air.[6]

The typical low concentration of these analytes in the atmosphere makes the detection and chemical characterization of particulate matter a challenge that can be taken over only by few analytical techniques of sensitivities as high as single particle resolution. For example, inductively coupled plasma mass spectrometry (ICPMS) in an approach named Single Particle-ICPMS.[7] Optical trapping (OT), introduced by Ashkin in the decade of 1970[8], is a simple yet efficient method of isolating individual airborne particles of sizes down to a few nanometers in diameter[9] by retaining them in controlled positions thanks to forces exerted on the particle by the radiation pressure of a tightly focused laser or in a combination of the aforementioned forces with gravity named optical levitation[10], OT allows manipulation of trapped particles in addition to probing in order to acquire a wide variety of information of individual specimens given the exceptional synergy it shows when combined with techniques like Raman spectroscopy.[11-12]

Coupling of OT and laser-induced breakdown spectroscopy (LIBS) mediated by optical catapulting (OC)[13-17] for single particle chemical characterization was first demonstrated by Fortes et al.[18] in the novel approach OC-OT-LIBS. LIBS is a well-stablished analytical technique that has been successfully applied for the analysis of aerosols[19-20] even in-situ[21], avoiding lengthy sample collection and preparation since the absolute mass required for LIBS analysis is extremely low, as reported in literature[22-24], and independent

from the physical state of the inspected samples. OC-OT-LIBS comprised the sequential intervention of its three consisting techniques: first, the shockwave generated from a laser pulse was used for optically catapulting sample particles into solid aerosol form which were individually trapped in consequence by an Ar^+ laser working at λ=514.5 nm. Lastly a Nd:YAG pulsed laser on its fundamental wavelength excited the particle in order to record the spectral emission from laser-induced plasmas of single particles such as 100 nm Al_2O_3. A limit of detection (LOD) of 200 attograms for Al was reported. The actual development stage of OC-OT-LIBS still requires the exploration of some of its features, particularly the factors conditioning the recorded signal and how it relates to particle size and mass. This question is encompassed in the present paper, where influence of energy density and acquisition delay on the LIBS spectra of 400 nm and 2 µm diameter single trapped graphite particles was studied in order to extract the efficiency of particle dissociation processes in the laser-produced plasma via the yield of photon per mass unit. The mechanism leading to particle excitation was concluded based on time-resolved plasma imaging results. Optical forces acting upon both types of particle size were estimated to characterize trapping stability. LOD of 1.7 fg for C was stablished.

2. Experimental

2.1 Instrument configuration

While the core description of the OC-OT-LIBS instrument can be found in a previous work,[18] several modifications, shown in **Figure 1A**, were introduced in the current study. For a simpler explanation on the distribution of the different lines comprising our setup, a Cartesian three-dimensional coordinate system, depicted in **Figure 1A**, is proposed. This system will be referred to throughout the paper for discussing matters like particle positioning as well (**Figure 1B**). Optical catapulting and particle excitation are located in the *x* axis. Both are performed by the same laser, a Q-switched Nd:YAG laser (1064 nm, 6 ns pulse width) guided into the sample-containing cuvette through two high reflectivity mirrors and a 10x high-power focusing objective (15 mm working distance, 0.25 N.A.). Material was catapulted into solid aerosol form by shockwaves from laser-induced plasmas. Such plasmas were ignited in air by the excitation laser. The shockwaves propagated along z axis and were energetic enough to eject the sample from the support upon impacting on it, filling the cuvette with suspended material. Also in this axis, a visualization line consisting of a compact USB 2.0 CMOS camera coupled to a 10x microscope objective (0.30 N.A.) was installed.

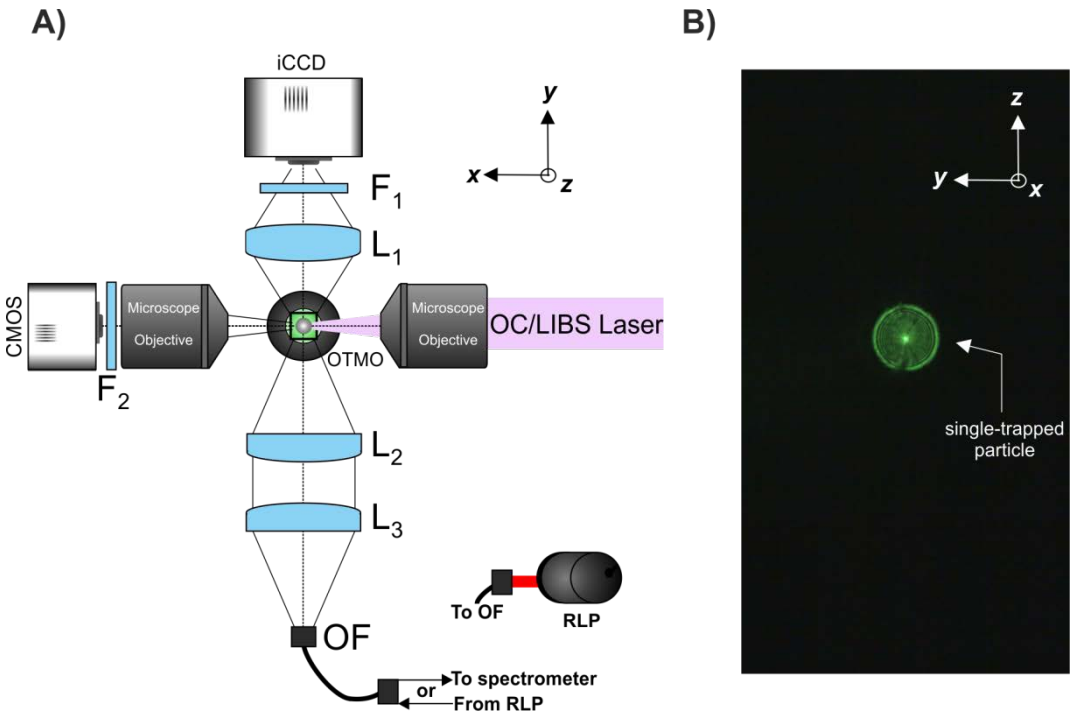

Figure 1. A) Experimental Setup. F_{1-2} are neutral density filters. L_{1-3} are focusing lenses. OF stands for optical fiber and OTMO, for optical trapping microscope objective. A 635 nm He-Ne red laser pointer (RLP) was used for the multi-alignment procedure. B) Individual particle positioned in the reference system as seen from the visualization line.

A neutral density filter was placed prior to the camera in order to reduce the intensity of light scattered by trapped particles. After aerosol production, single particles were successfully trapped in air at atmospheric pressure along the z axis by a CW Nd:YAG laser (532 nm, TEM 00) with a power of 300 mW directed to the back aperture of a 20x objective (17.5 mm working distance, 0.40 N.A.). Once isolated at several mm from the support and cuvette walls, particles were excited by single 1064 nm laser shots. Emission from the onset plasma was recorded in the y axis. Plasma light was simultaneously focused into an iCCD camera by a biconvex lens (UV-FS, 25.4 mm diameter, 50 mm focal length) for imaging analysis and by two plano-convex lenses (UV-FS, 50.8 mm diameter, 100 mm focal length) into the tip of an optical fiber (2m length, 600 µm diameter, 0.22 NA) connected to a time-integrated spectrometer for LIBS spectra. Neutral density filters covering a variety of attenuation coefficients could be placed before the iCCD camera if needed. 1064 nm laser action and energy were controlled by a pulse generator. A second pulse generator was used to set the delay between the laser pulse and spectrometer acquisition gate.

2.2 Multi-alignment scheme

A multi-step routine based on the iCCD camera was developed for ensuring the precise alignment of every system component. This procedure is graphically sketched in **Figure 2**. First, an image of clean air plasma was recorded. The image provided the exact location in the xz plane where the particle had to be situated for it to be intercepted by the excitation laser. Light scattered by a trapped particle was then observed in real time to evaluate its position. By moving the 20x objective along the z axis, the particle was manipulated until placed in the correct position, which marked the origin of our reference system i.e. the (0,0,0) coordinates. Lastly, LIBS detection was aligned by detaching the optical fiber's end connected to the spectrometer and passing a red laser pointer through it, traversing the collected light inverse path into the cuvette and reaching the camera.

2.3 Samples

Two different diameter graphite particles were used for the conducted studies: 2 µm (volume: 3.4 x 10^{-11} cm^3, mass: 9 pg, Sigma-Aldrich, dispersity: 2-12 µm) and 400 nm (volume: 3.3 x 10^{-14} cm^3, mass: 75 fg, MKNano). Sample powder was directly deposited on 200 µm thick glass slides and covered with a standard 10 mm path length disposable plastic cuvette, which prevented loss due to blowing from surrounding air.

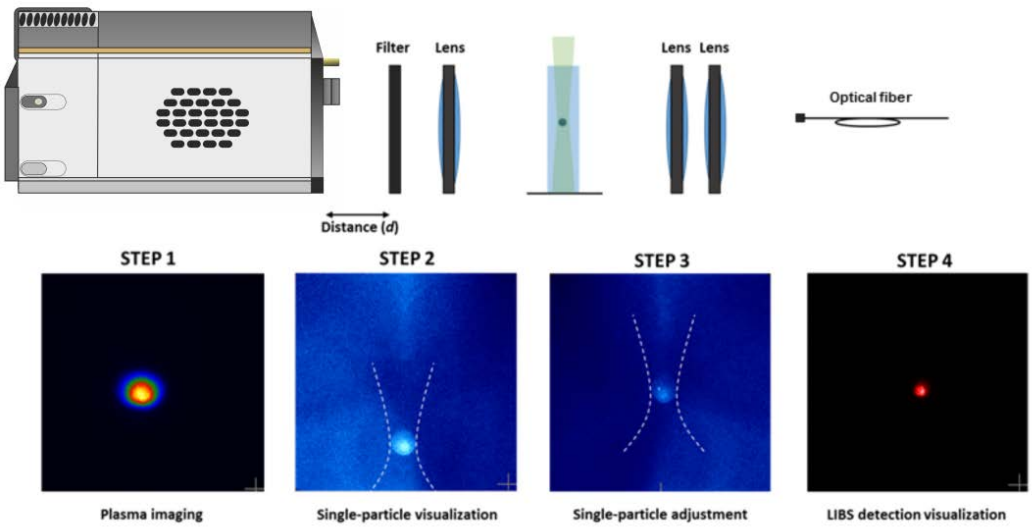

Figure 2. Sketch of the multi-alignment procedure.

3. Results and discussion

3.1 Optical trap stability

The optical trap developed here is robust enough for trapped particles to withstand collisions with other particles from the catapulted solid aerosol until complete relaxation, to allow monodimensional manipulation along the trapping laser axis, and, lastly, to keep the particle position during the parameters setting routine preceding the analysis (<1 min, usually). The system allowed particles of 2 microns and 400 nm to be suspended for periods longer than 8 hours in air at room temperature. Multiple particles could be retained along the z axis, but only those resting at the equilibrium position of the trap (xe, ye, ze) would remain long enough to be interrogated by further inspection techniques.

For a better understanding of the forces acting on the particles, the trap strength was calculated on the basis of the Equipartition theorem. While other methods have been used to calculate optical forces acting on trapped graphite particles due to a focused laser beam,[25] the present formalism considers a particle to be an oscillator in a harmonic potential, whose particle Brownian motion can be registered to calculate the trap stiffness, k, from the general expression:

$$\frac{1}{2}K_B T = \frac{1}{2}k\langle x^2\rangle \qquad \textbf{(Eq. 1)}$$

Where K_B is the Boltzmann constant and $\langle x^2\rangle$ is the variance of the particle displacement from its equilibrium position (x_e). Despite being a widely used simple calibration method, the Equipartition theorem may underestimate rigidity of traps given its dependence on $\langle x^2\rangle$.[26] The software developed by Osterman[27] employs Boltzmann statistics to diminish the inherent imprecision of Equation 1 and was therefore used to process our data. Particle coordinates were extracted from videos recorded using the visualization camera after every captured frame was converted to image format by running a custom made script for ImageJ software.[28] The resulting data matrix units were converted from pixels to µm and then used as input data. Since images provide 2D information, only two constants could be estimated: k_z and k_y. **Table 1** summarizes the spring constant values and z_e equilibrium position. As seen, the trapping strength for 2 µm particles is twofold that for 400 nm ones, whereas the lateral stiffness (k_y) exceeds its axial homologous (k_z) by two orders of magnitude.

Greater trap stiffness in the direction perpendicular to the beam propagation was expected since the gradient force (F_{grad}) originating from the light intensity gradient along the laser focusing region is stronger than other optical forces in this direction. The gradient force is a stabilizing force that holds the particle by attracting it to the intensity maximum.

In contrast, the extinction force, (F_{ext}), originated through momentum transfer from incident photons, pushes the particle out of the trap. Two processes contribute to F_{ext}, namely, absorption (F_{abs}) and, to a larger extent, scattering (F_{scat}). F_{ext} gains relevance in the trapping axis essentially because of the refractive index difference existing between graphite and air ($n_{graphite}$ =2.69;[29] n_{air}=1.00), which leads to increased scattering cross section of the particle. Also, due to absorption at 532 nm, photophoretic forces (F_{PP}) appearing from surface temperature differences are not negligible and add an instability factor.[30] In optical levitation traps, gravity counteracts F_{ext} besides F_{PP} and balance between the three forces determines the system equilibrium position. On a 2 µm graphite particle, gravity exerts an attraction of F_g = mg =9.34 x 10^{-14} N (g = 9.81 ms^{-2}). The similarity of this attraction force to the stiffness k_z (10^{-14} N μm^{-1}) explains the trapping of these particles. The reduced gravity force for 400 nm (F_g =7.33 x 10^{-16} N) implies greater ascending forces in this case. As a result, their equilibrium position is further from the laser focus, hence the weaker trap stiffness, quoted in **Table 1**.

3.2 Fine tuning of the spectroscopic signal

Every individual particle may be subjected to breakdown only once. The restriction of working in single-shot regime imposes the necessity of thoroughly controlling each of the factors conditioning the formation of laser-induced plasmas and the recording of its emission as significant shot-to-shot variability is tied to this specific kind of analysis. The role of excitation laser energy in OC-OT-LIBS was largely discussed in ref. **18**. Energy density on the particle and acquisition delay effects will be detailed in depth in the following subsections.

Table 1. Spring constants and z equilibrium position for both employed samples.

Particle diameter (µm)	k_z (N m^{-1})	k_y (N m^{-1})	z_e (µm)
2.0	5.11 x 10^{-8}	3.67 x 10^{-6}	137.7
0.4	2.63 x 10^{-8}	1.71 x 10^{-6}	155.0

3.2.1 Fluence

Plasma formation threshold of graphite particles was found to be above that of air. Typical required excitation energies were in the order of hundreds of mJ, involving high fluences ($\mathrm{F} \equiv \mathrm{J\ cm^{-2}}$). Under these experimental conditions, and given the extremely small sample mass available, air may become a major interference in LIBS spectra. The displacement of the excitation laser focusing objective along the x axis (see **Figure 1**) allowed control over the fluence at the origin of coordinates.

A systematic study was conducted on 2 µm particles in order to determine the position where plasma formation leaded to the most intense graphite signals while minimizing those emitted by air. In the reference system used for the study, the laser focus position (LFP) was sequentially modified from the particle position (LFP = 0 mm) for a total of 3 mm: 1.5 mm before (negative side of the x axis) and after (positive side of the x axis) the particle. The pulse energy used was 260 mJ. At each position 10 spectra were acquired with the control emissions being CN at 388.3 nm for graphite and N (II) at 399.5 nm for air. Monitoring of the CN band was considered once CN emission from sources other than the particle was discarded by recording spectra from empty traps. Plasma light collection was aligned at the (0,0,0) position in order to register light emitted only from the particle position. **Figure 3** shows the intensity variation for each LFP. CN signal improved the more un-focused the pulse was at the particle surface. Laser events at LFP = 0 mm generated exclusively air emission whereas at LFP = -1.5, the most favorable in terms of SNR ratio, clear graphite signal was recorded with largely reduced presence of N(II).

The signal distribution corroborated that the core of the plasma was mainly composed of air regardless of the LFP at which it was generated. Emissions from ionized air concealed those contributed by the particle at LFPs near 0 since the plasma core got progressively closer to the light collection. Fluence at (0,0,0) was estimated at 47 J cm^{-2} when LFP = -1.5 mm, an order of magnitude below F for LFP = 0 mm (832 J cm^{-2}). LFP = -1.5mm was considered the optimum position for particle excitation. The relative standard deviation (RSD) of this first tuning phase results ranged from 30 % to 50 %. When 400 nm particles were subjected to the same procedure, similar signal distributions were registered. Delimitation of the laser focus position range increased sampling efficiency to a 100% for both sized particles.

3.2.2 Acquisition delay

Delay (d) yielding the highest SNR for CN emission at 388.3 nm was determined by acquiring 2 µm graphite spectra at LFP = +1.5 mm. Despite the lower CN intensity, this position provided more sensitivity to delay during the first two microseconds, allowing a better evaluation of the parameter. When the experiment was repeated for other key LFP settings (0 and -1.5 mm), spectra showed identical trend. Delay was increased starting from its minimum possible value of 1.28 µs (considered as d = 0). Data were recorded every 1 µs from d = 0 to d = 11 µs, when the lapse was increased to 5 µs until plasma completely extinguished. **Figure 4** shows the variation of intensities with the delay. After the first microsecond, background and N (II) declined largely and CN became the most intense signal. Although graphite intensity peaked at a slightly shorter delay (3 µs), the best SNR was observed at 4 µs (corresponding to a SNR value of 14, as estimated from data in **Figure 4**).

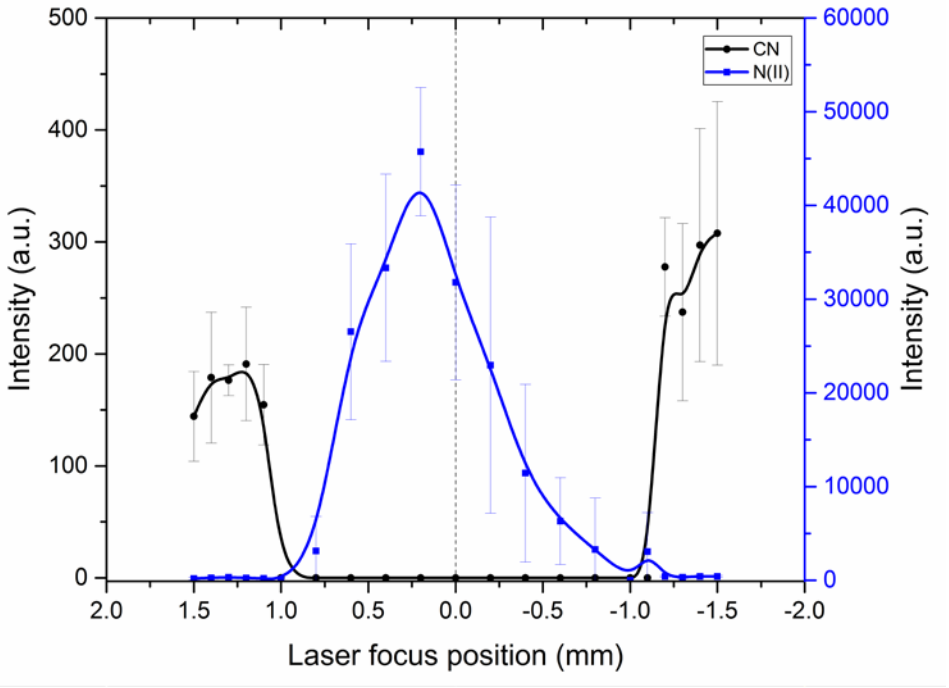

Figure 3. CN (388.3 nm) and N (II) (399.5 nm) net intensity distribution versus LFP along the x axis. Data are shown every 0.1 mm from ±1.5 mm to ±1.00 mm and every 0.2 mm from ±0.8 to 0 mm. Each point is the average of ten individual laser events on ten different single particles. Light collection was kept at 0 mm.

Again, the best experimental conditions were equivalent for 400 nm particles. RSD suffered a noteworthy improvement following collection delay optimization, going down from over 30% to 10% on 2 μm particles and 19% for 400 nm ones. The larger variability for 400 nm particles is due to optical forces sometimes pushing particle slightly out of the (0,0,0) position in the lateral direction, preventing it from being excited in the exact same way in every laser event. Optimized spectra allowed stablishing a LOD for graphite of 1.7 femtograms.

3.3 Mechanisms leading to particle dissociation in OC-OT-LIBS

It should be noted that irradiating the particle after decreasing the energy until F = 47 J cm^{-2} at LFP = 0 resulted in the absence of plasma formation since it was far below the calculated plasma ignition threshold of air (F = 255 J cm^{-2}). This fact suggests that, instead of a direct particle excitation by the incoming laser beam, particle breakdown results from a secondary ionization process caused by the plasma formed in air, in agreement with the observations by Hohreiter and Hahn[31] and Järvinen and Toivonen.[32] In Reference **31**, it is suggested that plasma first formed in air may serve as excitation source by engulfing the particle in its expansion, with the plasma-particle interaction dominating the evaporation process without direct laser pulse-particle interaction. Their hypothesis was evidenced by time resolved plasma imaging, which clearly located the particle under analysis in the plasma volume by local perturbations induced in the plasma properties. Plasma-particle interactions[33] are governed by heat transfer rates (from the plasma to the particle) and mass transfer rates (from the particle to the plasma) and are especially relevant if the excitation pulse rise time is short and the particle diameter is small,[34] as in the present study. In order to verify that the conclusions drawn from the aforementioned studies on the role of air plasma in particulate material dissociation and ionization were also applicable in our present work, time-resolved imaging was used by recording 1:1 images of particle plasmas every 100 ns with an integration time of 5 ns at LFPs 1.5, 0.0 and -1.5 mm. The results of this study are shown in **Figure 5**. Morphology of the plume development was nearly identical to that described by Amodeo et al. for air,[35] with the initial almost circular shape becoming elongated within 100 ns. As observed in the image sequence acquired for LFP = -1.5 mm, the front end of the forward-propagating air plasma reaches the particle in position (0,0,0) after ca. 200 ns. However, the backward front of the plasma formed at LFP = +1.5 mm takes more than 900 ns to reach the particle.

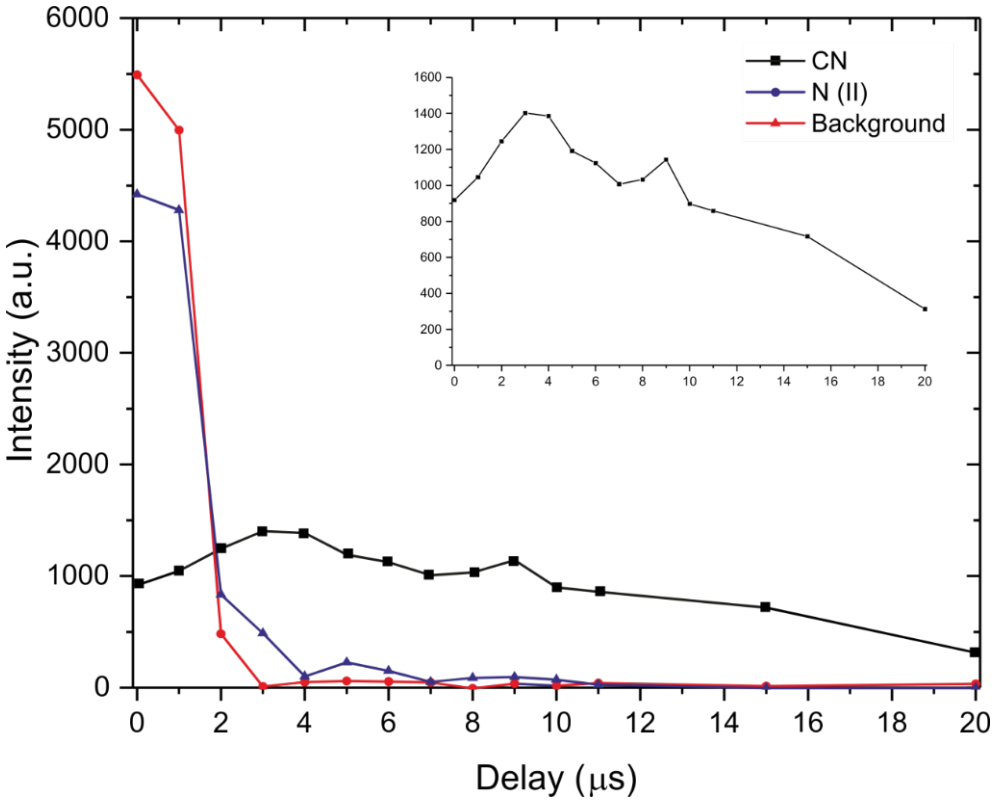

Figure 4. Net N (II) and CN signals temporal evolution plotted along spectral background for each delay. Data was acquired a LFP = +1.5 mm. Inset shows CN trend in greater detail.

Since the propagating plasma loses energy with time, the energy available for particle excitation is lower in the second case. This observation is consistent with the smaller intensity of the emissions shown in Figure 3 when the laser focus position is 1.5 mm beyond the particle (ca. 150 units) as compared to the intensity for LFP of -1.5 mm (ca. 300 units). Based on findings from literature and the discussed results, we conclude that the particle may be dissociated and excited by the plasma formed in air when LFP ≠ 0 mm.

The velocity of plasma expansion has been measured as a function of distance by analyzing plume images acquired at various delay times. **Figure 6** shows the results up to 7 μs at LFP = -1.5 mm. During the first 500 ns, the speed decreases exponentially and then, the propagation speed drops until the final collapse of the plume. When intercepting the particle, the plasma front propagates at roughly 1250 m/s. The role of the levitated particle on the plume expansion and whether the sudden decrease in propagation speed and distance traveled after the first microsecond is due to the natural energy lose by collisions with the surrounding air or to collisions with the levitated particle remain to be known.

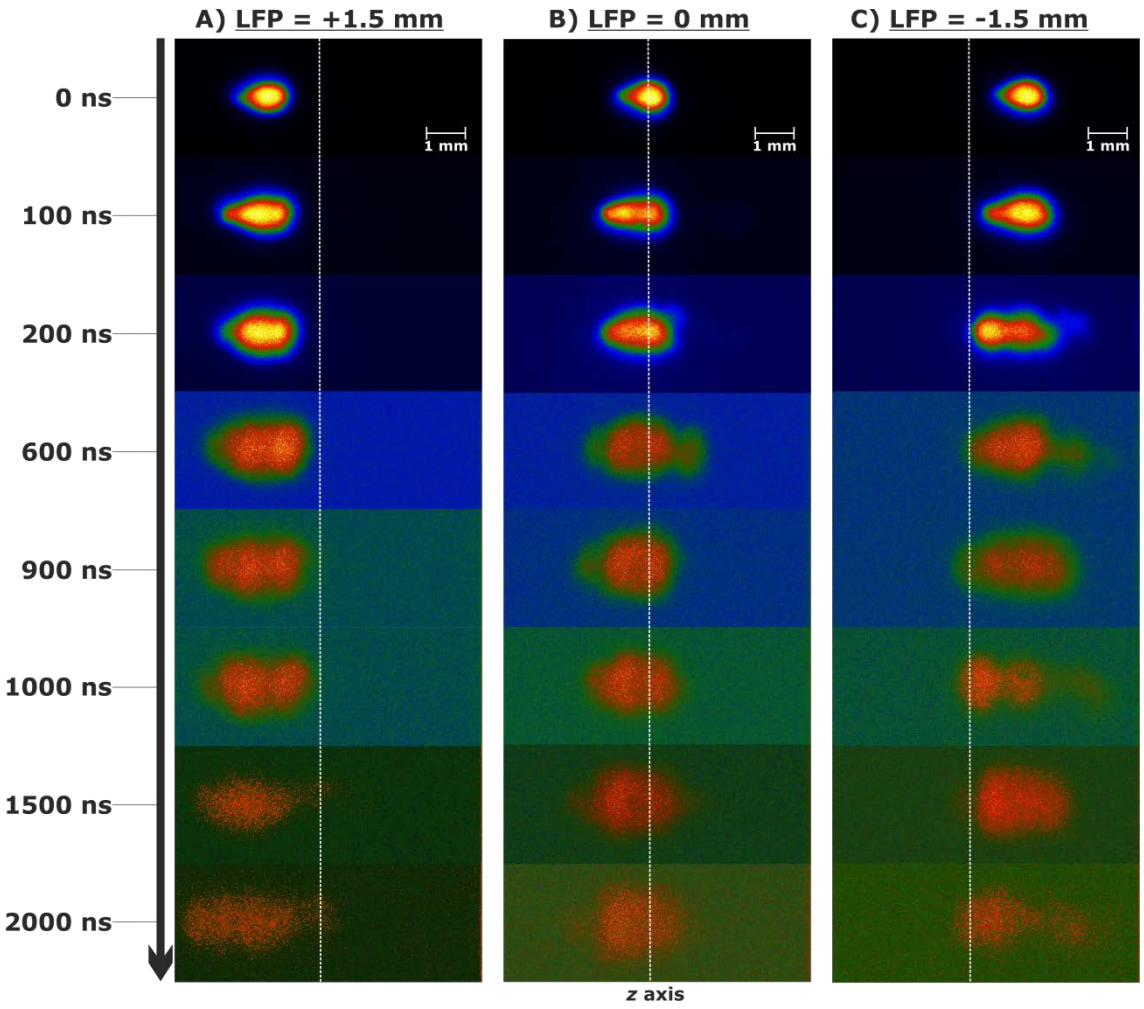

Figure 5. Single particle time-resolved plasma images acquired at laser focus positions: A) +1.5 mm; B) 0 mm; C) -1.5 mm. The laser propagates horizontally from the right. With an integration time of 5 ns, the acquisition delay was incremented in 100 ns steps. In each set of images, the white dashed line marks the axis where the particle is located. Image contrast was adjusted as required to highlight plasma emission against background.

3.4 Atomization efficiency and photon yield as a function of particle size

In addition to the well-known dependence of the LIBS signal on the ablated mass, when working on particulate material, particle size becomes a crucial parameter as it determines the efficiency of the dissociation processes. Carranza and Hahn denoted spherical SiO_2 particles signal intensity loss of linearity with respect to the particle mass for sizes greater than 2.1 µm, which they set as the upper limit for complete particle evaporation.[36] This threshold was calculated to be 5 µm for particles containing an elevated percentage of carbon.[37]

In our previous work, the number of photons produced in single laser events per mass unit was calculated for particles of diverse diameters and an inverse relation between

size and photon yield was established, albeit particle compositions also differed. The same method was employed for calculating the yield in our current experiment. Briefly, the number photons needed to generate a count of signal in the spectrometer was estimated alluding to the equation:

$$S = \frac{\omega_d}{Q_E\,\psi} \quad \textbf{(Eq. 2)}$$

Equation 2, relates the sensitivity S to the pixel well depth, ω_d, the quantum efficiency, Q_E, and the 16-bit AD converter, ψ. Then, tracking the light back to its source of generation, i.e. the particle, and accounting the optical elements it travels across, the photons causing the recorded signal were calculated along the production per mass unit. **Table 2** summarizes the results for the particles of interest. Twenty spectra per particle size were averaged. As observed, 400 nm particles yielded a photon count per mass unit larger than the 2 µm particles by more than two orders of magnitude. This fact is straightforwardly linked to the particle atomization efficiency.

Depending on the LFP at which a particle is excited, two different regimes lead to its dissociation: pulse-particle interaction (LFP = 0 mm) or, as discussed in section 3.3, plasma-particle interaction (LFP ≠ 0 mm). In the first case, radiation pressure and temperature buildup in the particle cause its eventual explosion. Taking into consideration the used pulse duration (6 ns), temperature plays a more prominent role than pressure.

Table 2. Spectroscopic yield of the tested particles.

Average particle diameter (µm)	Mass (g)	Mean net I (cts)	Intensity per mass unit (cts g^{-1})	Photon yield (photons g^{-1})
2.0	9.34×10^{-12}	1311	1.39×10^{14}	2.72×10^{18}
0.4	7.47×10^{-14}	1090	1.46×10^{16}	2.78×10^{20}

Heating does not occur at constant volume; both size particles have enough time to expand as the process takes place after the material characteristic time of mechanical relaxation,[38] given by the expression:

$$\tau = \frac{r_p}{c_p} \quad \textbf{(Eq. 3)}$$

Where τ is the mechanical relaxation time; r_p, is the particle radius and c_p, is the speed of sound in the particle, assumed to be 1470 m s^{-1} as in bulk graphite. Mechanical relaxation time was τ = 680 ps for 2 µm particles and τ = 136 ps for 400 nm particles. In explosions due to overheating, fragments are barely scattered[38] and can interact directly with the ongoing pulse. Since the laser penetrates deeper into 400 nm particles, a larger number of smaller, easier to excite, fragments results from their dissociation.[39] In the plasma-particle interaction regime, energy transferred from the plasma to the particle prompts the formation of fragments, which are subsequently excited by the same plasma. The larger surface area of 400 nm particles favors a closer interaction with the plasma, thus resulting in an extended dissociation process. Given the lower particle mass and constituent atom number, less energy needs to be employed for its disintegration and can, in turn, be invested in increasing the excitation efficiency, hence the higher number of photons emitted by these particles.

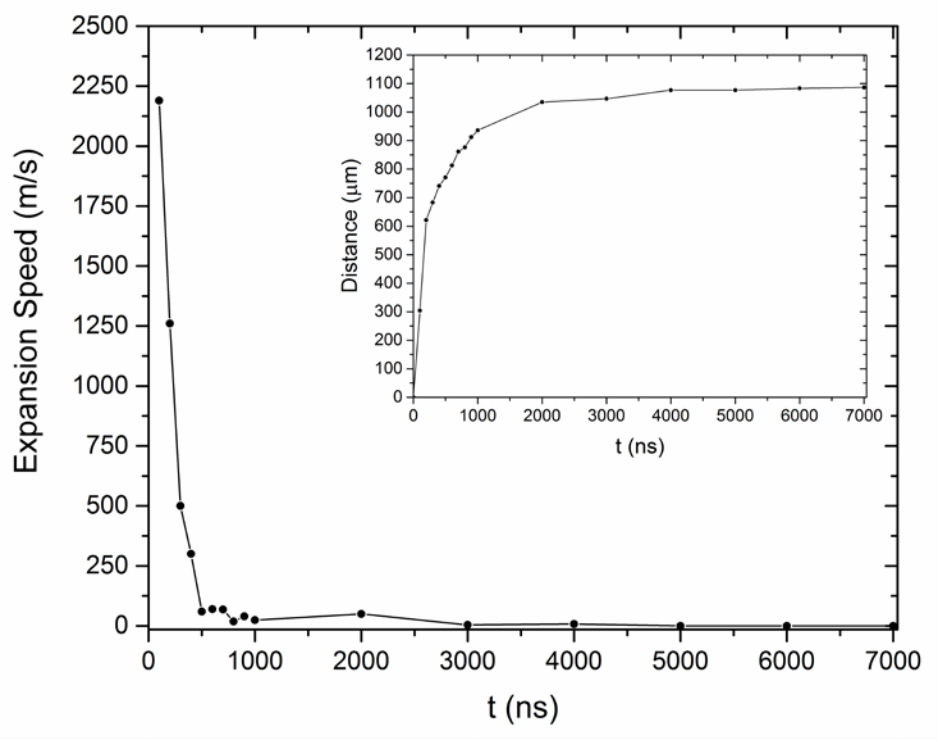

Figure 6. Expansion speed calculated for plasma formed at LFP = -1.5. For the first 500 ns, the decrease is exponential, turning into an almost flat trend from there onwards. Inset displays the distance traveled by plasma front during the measured time lapse.

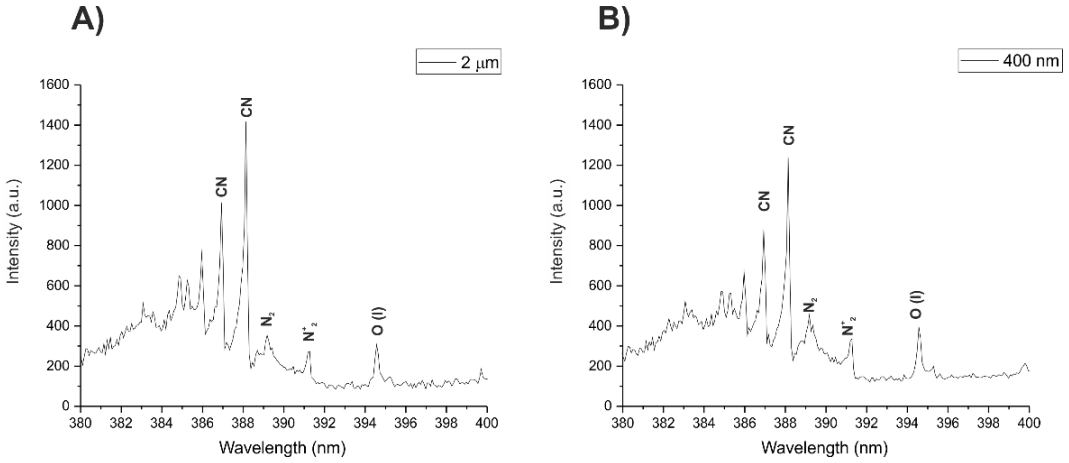

Figure 7. Average spectra of 20 A) 2 µm and B) 400 nm particles at LFP = -1.5 mm, d = 4 µs.

Figure 7 shows spectra for both particle sizes. Despite the two orders of magnitude separating the mass of both particles, there is scarce difference among recorded intensities, pointing towards a maximum size for total dissociation of graphite particles existing in the 400 nm-2 µm diameter interval under our experimental conditions to be explored in the future by expanding the range of sizes under study.

4. Conclusions

LIBS was successfully applied for analysis of single airborne graphite solid particles of 400 nm diameter isolated in optical traps with a 100% sampling efficiency. After a multi-alignment procedure to ensure correct positioning of particles and instrument components, the trapping strength was determined by calculating the trap stiffness. Despite the low optical forces being exerted on the particles, trapping was possible due to these forces being in the same order of magnitude of counterbalancing gravity attraction. Particles were found to undergo dissociation and excitation via two different mechanisms as proposed in LIBS bibliography following time-resolved plasma imaging studies: direct laser pulse-particle interaction and plasma-particle interaction, where the particle is evaporated by energy transferred from the expanding air plasma. Absolute production of photons per sample mass unit was calculated for each particle size, corresponding to masses of 9 pg (2 µm) and 75 fg (400 nm). The larger particles emitted 2.72×10^{18} photons per gram, whereas 75 fg particles yielded 2.78×10^{20} photons g^{-1}, pointing a more efficient dissociation of the smaller sizes which can be attributed to higher fragmentation of 400 nm particles due to the closer particle-plasma interaction taking place in the optical trap.

Acknowledgments

Research funded by the Spanish Ministerio de Economia y Competitividad under Project CTQ2014-56058P. P. Purohit gratefully acknowledges the concession of a FPI grant associated to the same project.

References

[1] Seaton, A., Godden, D., MacNee, W. & Donaldson, K. *"Particulate air pollution and acute health effects"*. Lancet **345**, 176–178 (1995).

[2] Brunekreef, B. & Holgate, S. T. *"Air pollution and health"*. Lancet **360**, 1233–1242 (2002).

[3] Castro, L. M., Pio, C. A., Harrison, R. M. & Smith, D. J. T. *"Carbonaceous aerosol in urban and rural European atmospheres: Estimation of secondary organic carbon concentrations"*. Atmos. Environ. **33**, 2771–2781 (1999).

[4] Jacobson, M. Z. *"Strong radiative heating due to the mixing state of black carbon in atmospheric aerosols"*. Nature **409**, 695–697 (2001).

[5] Menon, S., Hansen, J., Nazarenko, L. & Luo, Y. *"Climate effects of black carbon aerosols in China and India"*. Science **297**, 2250–2253 (2002).

[6] Borm, P. J. A., Robbins, D., Haubold, S., Kuhlbusch, T., Fissan, H., Donaldson, K., Schins, R., Stone, V., Kreyling, W., Lademann, J., Krutmann, J., Warheit, D. B. & Oberdorster, E. "*The potential risks of nanomaterials: A review carried out for ECETOC*". Particle and Fibre Toxicology vol. 3 (2006).

[7] Laborda, F., Bolea, E. & Jiménez-Lamana, J. *"Single particle inductively coupled plasma mass spectrometry: A powerful tool for nanoanalysis"*. Anal. Chem. **86**, 2270–2278 (2014).

[8] Ashkin, A. *"Acceleration and Trapping of Particles by Radiation Pressure"*. Phys. Rev. Lett. **24**, 156–159 (1970).

[9] Jauffred, L., Taheri, S. M. R., Schmitt, R., Linke, H. & Oddershede, L. B. *"Optical Trapping of Gold Nanoparticles in Air"*. Nano Lett. **15**, 4713–4719 (2015).

[10] Ashkin, A. & Dziedzic, J. M. *"Optical levitation by radiation pressure"*. Appl. Phys. Lett. **19**, 283–285 (1971).

[11] McGloin, D., Burnham, D. R., Summers, M. D., Rudd, D., Dewar, N. & Anand, S. "*Optical manipulation of airborne particles: techniques and applications*". Faraday Discuss. **137**, 335–350 (2008).

[12] Redding, B., Schwab, M. & Pan, Y. Le. *"Raman spectroscopy of optically trapped single biological micro-particles"*. Sensors (2015).

[13] Fortes, F. J., Cabalín, L. M. & Laserna, J. J. *"Laser-induced breakdown spectroscopy of solid aerosols produced by optical catapulting"*. Spectrochim. Acta - Part B At. Spectrosc. **64**, 642–648 (2009).

[14] Fortes, F. J. & Laserna, J. J. *"Characteristics of solid aerosols produced by optical catapulting studied by laser-induced breakdown spectroscopy"*. Appl. Surf. Sci. **256**, 5924–5928 (2010)

[15] Abdelhamid, M., Fortes, F. J., Harith, M. A. & Laserna, J. J. *"Analysis of explosive residues in human fingerprints using optical catapulting-laser-induced breakdown spectroscopy"*. J. Anal. At. Spectrom. (2011).

[16] Abdelhamid, M., Fortes, F. J., Laserna, J. J. & Harith, M. A. *"Optical Catapulting Laser Induced Breakdown Spectroscopy (OC-LIBS) and conventional LIBS: A comparative study"*. AIP Conference Proceedings (2011).

[17] Abdelhamid, M., Fortes, F. J., Fernández-Bravo, A., Harith, M. A. & Laserna, J. J. *"Production of aerosols by optical catapulting: Imaging, performance parameters and laser-induced plasma sampling rate"*. Spectrochim. Acta Part B At. Spectrosc. **89**, 1–6 (2013).

[18] Fortes, F. J., Fernández-Bravo, A. & Javier Laserna, J. *"Chemical characterization of single micro- and nano-particles by optical catapulting-optical trapping-laser-induced breakdown spectroscopy"*. Spectrochim. Acta - Part B At. Spectrosc. **100**, 78–85 (2014).

[19] Hahn, D. W. & Lunden, M. M. *"Detection and analysis of aerosol particles by laser-induced breakdown spectroscopy"*. Aerosol Sci. Technol. (2000).

[20] Álvarez-Trujillo, L. A., Ferrero, A. & Javier Laserna, *"J. Preliminary studies on stand-off laser induced breakdown spectroscopy detection of aerosols"*. J. Anal. At. Spectrom. (2008).

[21] Hettinger, B., Hohreiter, V., Swingle, M. & Hahn, D. W. *"Laser-induced breakdown spectroscopy for ambient air particulate monitoring: Correlation of total and speciated aerosol particle counts"*. Appl. Spectrosc. (2006).

[22] Zorba, V., Mao, X. & Russo, R. E. *"Ultrafast laser induced breakdown spectroscopy for high spatial resolution chemical analysis"*. Spectrochim. Acta - Part B At. Spectrosc. **66**, 189–192 (2011).

[23] Diwakar, P. K., Loper, K. H., Matiaske, A.-M. & Hahn, D. W. *"Laser-induced breakdown spectroscopy for analysis of micro and nanoparticles"*. J. Anal. At. Spectrom. **27**, 1110 (2012).

[24] Järvinen, S. T., Saari, S., Keskinen, J. & Toivonen, J. *"Detection of Ni, Pb and Zn in water using electrodynamic single-particle levitation and laser-induced breakdown spectroscopy"*. Spectrochim. Acta - Part B At. Spectrosc. **99**, 9–14 (2014).

[25] Eckerskorn, N., Bowman, R., Kirian, R. A., Awel, S., Wiedorn, M., Küpper, J., Padgett, M. J., Chapman, H. N. & Rode, A. V. "*Optically Induced Forces Imposed in an Optical Funnel on a Stream of Particles in Air or Vacuum*". Phys. Rev. Appl. **4**, 1–14 (2015).

[26] Neuman, K. C. & Block, S. M. *"Optical trapping"*. Review of Scientific Instruments (2004).

[27] Osterman, N. *"TweezPal - Optical tweezers analysis and calibration software"*. Comput. Phys. Commun. **181**, 1911–1916 (2010).

[28] Abràmoff, M. D., Magalhães, P. J. & Ram, S. J. *"Image processing with imageJ"*. Biophotonics International **11**, 36-42 (2004).

[29] Djurisic, A.B. & Li, E.H. *"Optical properties of graphite"*, J. Appl. Phys. **85** 7404-7410 (1999).

[30] Beresnev, S., Chernyak, V. & Fomyagin, G. *"Photophoresis of a spherical particle in a rarefied gas"*. Phys. Fluids A Fluid Dyn. **5**, 2043–2052 (1993).

[31] Hohreiter, V. & Hahn, D. W. *"Plasma-particle interactions in a laser-induced plasma: Implications for laser-induced breakdown spectroscopy"*. Anal. Chem. **78**, 1509–1514 (2006)

[32] Järvinen, S. T. & Toivonen, J. *"Analysis of single mass-regulated particles in precisely controlled trap using laser-induced breakdown spectroscopy"*. Opt. Express **24**, 1314 (2016).

[33] Hahn, W. D. & Omenetto, N. *"Laser-Induced Breakdown Spectroscopy (LIBS), Part I: Review of Basic Diagnostics and Plasma-Particle Interactions: Still-Challenging Issues Within the Analytical Plasma Community"*. Appl. Spectrosc. **64**, 335A-366A (2010).

[34] Warren, R.A. *"Laser Induced Breakdown Spectroscopy on Suspended Particulate Matter in an Electrodynamic Balance: Interaction Processes and Analytical Considerations, PhD thesis"*, University of Florida (2013).

[35] Amodeo, T., Dutouquet, C., Le Bihan, O., Attoui, M. & Frejafon, E. *"On-line determination of nanometric and sub-micrometric particle physicochemical characteristics*

using spectral imaging-aided Laser-Induced Breakdown Spectroscopy coupled with a Scanning Mobility Particle Sizer". Spectrochim. Acta - Part B At. Spectrosc. **64**, 1141–1152 (2009).

[36] Carranza, J. E. & Hahn, D. W. *"Assessment of the Upper Particle Size Limit for Quantitative Analysis of Aerosols Using Laser-Induced Breakdown Spectroscopy"*. Anal. Chem. **74**, 5450–5454 (2002).

[37] Vors, E. & Salmon, L. *"Laser-induced breakdown spectroscopy (LIBS) for carbon single shot analysis of micrometer-sized particles"*. Anal. Bioanal. Chem. **385**, 281–286 (2006).

[38] Zhigilei, L. V. & Garrison, B. J. *"Computer simulation study of damage and ablation of submicron particles from short-pulse laser irradiation"*. Appl. Surf. Sci. **127**–**129**, 142–150 (1998).

[39] Schoolcraft, T. A., Constable, G. S., Zhigilei, L. V. & Garrison, B. J. *"Molecular Dynamics Simulation of the Laser Disintegration of Aerosol Particles"*. Anal. Chem. **72**, 5143–5150 (2000).